

Contraction Rate and Its Relationship to Frontogenesis, the Lyapunov Exponent, Fluid Trapping, and Airstream Boundaries

ROBERT A. COHEN

Department of Physics, East Stroudsburg University, East Stroudsburg, Pennsylvania

DAVID M. SCHULTZ

Cooperative Institute for Mesoscale Meteorological Studies, University of Oklahoma, and NOAA/National Severe Storms Laboratory, Norman, Oklahoma

(Manuscript received 2 June 2004, in final form 25 October 2004)

ABSTRACT

Although a kinematic framework for diagnosing frontogenesis exists in the form of the Petterssen frontogenesis function and its vector generalization, a similar framework for diagnosing airstream boundaries (e.g., drylines, lee troughs) has not been constructed. This paper presents such a framework, beginning with a kinematic expression for the rate of change of the separation vector between two adjacent air parcels. The maximum growth rate of the separation vector is called the instantaneous dilatation rate and its orientation is called the axis of dilatation. Similarly, a maximum decay rate is called the instantaneous contraction rate and its orientation is called the axis of contraction. These expressions are related to the vector frontogenesis function, in that the growth rate of the separation vector corresponds with the scalar frontogenesis function, and the rotation rate of the separation vector corresponds with the rotational component of the vector frontogenesis function.

Because vorticity can rotate air-parcel pairs out of regions of deformation, the instantaneous dilatation and contraction rates and axes may not be appropriate diagnostics of airstream boundaries for fluid flows in general. Rather, the growth rate and orientation of an airstream boundary may correspond better to the so-called asymptotic contraction rate and the asymptotic axis of dilatation, respectively. Expressions for the asymptotic dilatation and contraction rates, as well as their orientations, the asymptotic dilatation and contraction axes, are derived. The asymptotic dilatation rate is related to the Lyapunov exponent for the flow. In addition, a fluid-trapping diagnostic is derived to distinguish among adjacent parcels being pulled apart, being pushed together, or trapped in an eddy. Finally, these diagnostics are applied to simple, idealized, steady-state flows and a nonsteady idealized vortex in nondivergent, diffusive flow to show their utility for determining the character of air-parcel trajectories and airstream boundaries.

1. Introduction

Interesting weather in the atmosphere often occurs along boundaries between different air masses. Fronts are one example of such boundaries, as flows with convergence and deformation concentrate isotherms at the edges of air masses. In conjunction with this frontogenesis, secondary horizontal and vertical ageostrophic circulations result to restore thermal-wind balance, as per geostrophic and semigeostrophic theory. Other examples of boundaries include drylines, lee troughs, and baroclinic troughs (Sanders 1999), features that are fundamentally characterized by abrupt changes in wind

speed and direction, but, unlike fronts, are not necessarily associated with, or characterized by, temperature gradients [see the discussion in section 2b of Cohen and Kreitzberg (1997) and in section 4 of Sanders (1999)]. We term these features *airstream boundaries* because airstreams having different origins are brought closer together to form boundaries in the flow.

A kinematic framework to diagnose frontogenesis in a Lagrangian sense (following air parcels) has a long history (e.g., Petterssen 1936; Miller 1948; Keyser et al. 1988; Keyser 1999). In contrast, whereas frameworks to study the coherence of airstreams have been developed (e.g., Carlson 1980; Browning 1986, 1990; Wernli and Davies 1997; Wernli 1997), quantitative approaches to diagnose the boundaries between airstreams have not been as extensively studied. One approach is that of Cohen and Kreitzberg (1997). They define the *average contraction rate* C as the time-averaged rate at which the three-dimensional distance between two adjacent

Corresponding author address: Dr. David M. Schultz, NOAA/National Severe Storms Laboratory, 1313 Halley Circle, Norman, OK 73069.
E-mail: david.schultz@noaa.gov

air-parcel changes over some previous finite time period t ending at $t = 0$:

$$C = -\frac{1}{t} \ln \left[\frac{r(t)}{r(0)} \right]; \quad t < 0, \quad (1)$$

where $r(t)$ is the distance between the two parcels at time t . Cohen and Kreitzberg (1997) calculate C by computing air-parcel trajectories from mesoscale model output over the entire model domain back in time 12 h. The distances between adjacent trajectories at their origins, $r(-12 \text{ h})$, and their final locations, $r(0)$, can then be used to calculate C as expressed in (1). As shown in Cohen and Kreitzberg (1997), regions of large positive 12-h average contraction rate are associated with airstream boundaries in a rapidly developing midlatitude cyclone. Thus, the average contraction rate can be used as a quantitative measure of the strength of an airstream boundary.

Such a diagnosis of average contraction rates, however, requires computing fluid-parcel trajectories, a computationally expensive process requiring specialized code. In addition, high temporal and spatial resolution may be needed, especially for diagnosing small-scale features. If, however, a kinematic expression for the contraction rate were possible, the development of airstream boundaries could be assessed without the temporal history needed to compute airstream boundaries using the approach of Cohen and Kreitzberg (1997).

The purpose of this paper is to develop an expression for the contraction rate using fundamental kinematic quantities. In section 2, expressions are derived for the instantaneous dilatation and contraction rates. These kinematic expressions are the maximum and minimum rates of change of the distance between two adjacent air parcels, respectively, and the instantaneous contraction rate is the instantaneous analog to the time-averaged contraction rate C . In addition, the instantaneous contraction rate is related to the expression for accumulation (Saucier 1955, section 10.39) and the frontogenesis function (Petterssen 1936; Keyser et al. 1988). The axis of dilatation represents the direction of maximum stretching of fluid parcels by the deformation in the flow. When vorticity is present in the flow, the vorticity will rotate air-parcel pairs from the regions of maximum instantaneous dilatation and contraction rates. Consequently, expressions for what we term the asymptotic dilatation and contraction rates are derived in section 3. The directions associated with the asymptotic dilatation and contraction rates are called the asymptotic dilatation and contraction axes, respectively. Where the asymptotic contraction rate is positive, the asymptotic dilatation axis represents the orientation of the instantaneous processes acting to create an airstream boundary. In addition, the asymptotic dilatation rate is related to the instantaneous local Lyapunov exponent. These derivations yield an intriguing expres-

sion for what we term the fluid-trapping diagnostic. This diagnostic is a measure of whether adjacent air parcels approach each other, separate from each other, or are trapped together in an eddy. Such a diagnostic can be used to assess whether the flow is characterized by straining or eddies. In a straining-dominated flow, adjacent air parcels approach or separate from each other. In contrast, in an eddy-dominated flow, the separation vector between adjacent air parcels oscillates in length and rotates, trapping the fluid inside the eddies. The fluid-trapping diagnostic has wider applications to turbulence, chaos, and predictability (e.g., McWilliams 1984; Benzi et al. 1988; Pierrehumbert and Yang 1993). The utility of these expressions is illustrated in section 4 by their application to an idealized, nondivergent flow resembling an extratropical cyclone in a diffluent jet-exit region, where regions of large asymptotic contraction rate correspond to airstream boundaries. The article concludes in section 5 with a summary and some possible applications of these kinematic expressions to observed atmospheric flows. Appendix A is a list of symbols found in this paper. A derivation of the instantaneous local Lyapunov exponent discussed in section 3 is presented in appendix B.

2. Instantaneous dilatation and contraction rates

Consider two fluid parcels separated by a vector distance $\delta \mathbf{r}(t)$, the infinitesimal vector analog to $r(t)$ in (1). Owing to gradients of fluid motion within the flow, the velocity of the two parcels may be different, leading to a change in their vector separation $\delta \mathbf{r}(t)$. If $\delta \mathbf{r}(t)$ changes quickly, trajectories of the fluid parcels would be highly dependent on their initial positions. Such sensitive dependence of parcel trajectories on their initial positions is characteristic of chaotic flow and has implications for the predictability of the flow.

To simplify analysis and interpretation, only horizontal motions are considered. To represent the time dependence of the separation in two dimensions between these two fluid parcels, the separation vector for a small period of time $\delta \mathbf{r}(t)$ is written in terms of a growth rate σ and rotation rate ω :

$$\delta \mathbf{r}(t) = \delta \mathbf{r}(0) \exp[(\sigma + i\omega)t], \quad (2)$$

where the real and imaginary parts of $\delta \mathbf{r}(t)$ can be viewed as components of a vector $(\delta x, \delta y)$:

$$\delta \mathbf{r}(t) = \delta x + i\delta y. \quad (3)$$

Written in this way, the magnitude of the separation vector would increase exponentially with time at a rate σ , and the separation vector would rotate with an angular frequency ω , positive for counterclockwise rotations.

These expressions can be solved for σ and ω , resulting in the growth rate and rotation rate of the separa-

tion vector throughout the flow for small times. From (3), the rate of change of the separation vector is

$$\frac{d(\delta\mathbf{r})}{dt} = \frac{d(\delta x)}{dt} + i \frac{d(\delta y)}{dt}.$$

A Taylor expansion over a small time period, retaining only the linear terms, yields

$$\frac{d(\delta\mathbf{r})}{dt} = \left(\frac{\partial u}{\partial x} \delta x + \frac{\partial u}{\partial y} \delta y \right) + i \left(\frac{\partial v}{\partial x} \delta x + \frac{\partial v}{\partial y} \delta y \right). \quad (4)$$

This is equivalent to the linear strain rate of a fluid element in each direction (e.g., Kundu 1990, 54–55). Doswell (1984) showed that the neighborhood of a point within which neglect of higher-order terms is valid is approximately one-tenth the horizontal scaling length.

Substituting (2) and (3) into (4) results in

$$(\sigma + i\omega)(\delta x + i\delta y) = \left(\frac{\partial u}{\partial x} \delta x + \frac{\partial u}{\partial y} \delta y \right) + i \left(\frac{\partial v}{\partial x} \delta x + \frac{\partial v}{\partial y} \delta y \right).$$

The expression has two parts, a real part and an imaginary part, resulting in two independent equations:

$$\sigma \delta x - \omega \delta y = \frac{\partial u}{\partial x} \delta x + \frac{\partial u}{\partial y} \delta y,$$

$$\sigma \delta y + \omega \delta x = \frac{\partial v}{\partial x} \delta x + \frac{\partial v}{\partial y} \delta y.$$

Substituting $\delta x = |\delta\mathbf{r}| \cos\phi$ and $\delta y = |\delta\mathbf{r}| \sin\phi$, where ϕ is the orientation of the parcel pair, yields

$$\sigma = \frac{\partial u}{\partial x} \cos^2\phi + \frac{\partial v}{\partial y} \sin^2\phi + \left(\frac{\partial u}{\partial y} + \frac{\partial v}{\partial x} \right) \sin\phi \cos\phi,$$

$$\omega = \frac{\partial v}{\partial x} \cos^2\phi - \frac{\partial u}{\partial y} \sin^2\phi + \left(\frac{\partial v}{\partial y} - \frac{\partial u}{\partial x} \right) \sin\phi \cos\phi.$$

Using trigonometric relationships, these expressions can be simplified to

$$\sigma = \frac{1}{2} (E_{\text{sh}} \sin 2\phi + E_{\text{st}} \cos 2\phi + D), \quad (5a)$$

$$\omega = \frac{1}{2} (E_{\text{sh}} \cos 2\phi - E_{\text{st}} \sin 2\phi + \zeta), \quad (5b)$$

where divergence $D = \partial u/\partial x + \partial v/\partial y$, relative vorticity $\zeta = \partial v/\partial x - \partial u/\partial y$ (hereafter referred to as vorticity), stretching deformation $E_{\text{st}} = \partial u/\partial x - \partial v/\partial y$, and shearing deformation $E_{\text{sh}} = \partial u/\partial y + \partial v/\partial x$.

In general, at each point in the flow, an orientation ψ_d exists for which the growth rate σ is largest, and an orientation ψ_c exists for which the growth rate is smallest. These maximum and minimum values of σ occur where

$$\left. \frac{d\sigma}{d\phi} \right|_{\phi=\psi_d} = \left. \frac{d\sigma}{d\phi} \right|_{\phi=\psi_c} = 0.$$

Solving the above equation leads to the following relationship:

$$\tan 2\psi_d = \tan 2\psi_c = \left(\frac{\partial v}{\partial x} + \frac{\partial u}{\partial y} \right) / \left(\frac{\partial u}{\partial x} - \frac{\partial v}{\partial y} \right) = E_{\text{sh}}/E_{\text{st}}. \quad (6)$$

The orientation ψ_d corresponds to the *axis of dilatation*, the orientation of maximum growth rate. The value of this maximum growth rate $\sigma|_{\phi=\psi_d}$ is termed *d*, the *instantaneous dilatation rate*. The other orientation ψ_c corresponds to the *axis of contraction*, the orientation at which the growth rate is a minimum. Correspondingly, the *instantaneous contraction rate c* is defined as the negative of the minimum growth rate (i.e., the maximum decay rate $-\sigma|_{\phi=\psi_c}$). The instantaneous contraction rate *c* is the instantaneous analog to the average contraction rate *C* in (1). Note that the two solutions to (6) must be orthogonal (i.e., $\psi_c = \psi_d + \pi/2$), because $\tan 2\phi = \tan 2(\phi + \pi/2)$. Thus, one orientation can be obtained via

$$\psi = \frac{1}{2} \tan^{-1} \left(\frac{E_{\text{sh}}}{E_{\text{st}}} \right), \quad (7)$$

and the other orientation can be obtained by adding $\pi/2$ to (7).

To rewrite the expressions for the growth and rotation rates (5a) and (5b) in terms of ψ (i.e., ψ_d and ψ_c), (6) can be expressed as

$$\sin 2\psi = \pm E_{\text{sh}}/E,$$

$$\cos 2\psi = \pm E_{\text{st}}/E,$$

where the resultant deformation $E = (E_{\text{st}}^2 + E_{\text{sh}}^2)^{1/2}$, and the two signs on the right-hand side correspond to the two values of ψ . As can be shown by taking the second derivative of σ with respect to ϕ , the positive value corresponds to ψ_d and the negative value corresponds to ψ_c . Using these expressions in (5a) and (5b), the deformation terms E_{sh} and E_{st} , which depend on the coordinate system, are replaced by the preferred Galilean-invariant resultant deformation E (hereafter, referred to simply as deformation):

$$\sigma = \frac{1}{2} (\pm E \sin 2\psi \sin 2\phi \pm E \cos 2\psi \cos 2\phi + D),$$

$$\omega = \frac{1}{2} (\pm E \sin 2\psi \cos 2\phi \mp E \cos 2\psi \sin 2\phi + \zeta).$$

Employing trigonometric identities yields

$$\sigma = \frac{1}{2} [\pm E \cos 2(\psi - \phi) + D], \quad (8a)$$

$$\omega = \frac{1}{2} [\pm E \sin 2(\psi - \phi) + \zeta]. \quad (8b)$$

It can be shown that σ in (8a) equals the negative of the partial derivative along an arbitrarily chosen direction of the projection of vector wind velocity onto the same direction. A similar relationship appears in the expressions for the frontogenesis function, as discussed later in section 2b.

When $\phi = \psi$, $\omega = \zeta$, implying that, for parcel pairs situated along the axes of dilatation or contraction, vorticity is the only process by which rotation of these parcel pairs occurs. In addition, when $\phi = \psi$, σ is either a maximum or minimum with the values:

$$\sigma|_{\phi=\psi} = \frac{\pm E + D}{2}, \quad (9)$$

respectively. The right-hand side of (9) is maximum when the sign is positive and minimum when the sign is negative, in agreement with the meaning identified earlier. Because the instantaneous dilatation rate is defined as the maximum growth rate d , and the instantaneous contraction rate is defined as the negative of the minimum growth rate c ,

$$d = \sigma|_{\phi=\psi_d} = \frac{E + D}{2}, \quad (10a)$$

and

$$c = -\sigma|_{\phi=\psi_c} = \frac{E - D}{2}. \quad (10b)$$

To simplify notation, the expressions in (8a) and (8b) for σ and ω , respectively, can be written in terms of ψ_d :

$$\sigma = \frac{1}{2}[E \cos 2(\psi_d - \phi) + D], \quad (11a)$$

$$\omega = \frac{1}{2}[E \sin 2(\psi_d - \phi) + \zeta]. \quad (11b)$$

The maximum counterclockwise (positive) or clockwise (negative) rotation rate occurs 45° between the axes of dilatation and contraction. Using (11b), these maximum and minimum rotation rates, Ω_+ and Ω_- , can be determined:

$$\Omega_{\pm} = \frac{\pm E + \zeta}{2}. \quad (12)$$

This equation shows that deformation increases the maximum rotation rate of the parcel pair over that due to vorticity alone. Likewise, deformation decreases the minimum rotation rate of the parcel pair over that due to vorticity alone.

a. Examples

To illustrate these expressions for some idealized flow patterns, consider a flow field:

$$\begin{aligned} u &= u_0 + \left(\frac{\partial u}{\partial x}\right)x + \left(\frac{\partial u}{\partial y}\right)y \\ &= \frac{1}{2}(u_0 + Dx + E_{sh}y + E_{st}x - \zeta y), \end{aligned} \quad (13a)$$

$$\begin{aligned} v &= v_0 + \left(\frac{\partial v}{\partial x}\right)x + \left(\frac{\partial v}{\partial y}\right)y \\ &= \frac{1}{2}(v_0 + Dy + E_{sh}x - E_{st}y + \zeta x), \end{aligned} \quad (13b)$$

where (u_0, v_0) represents a uniform translation. Here, we assume that the derivatives of the wind field, as well as $u_0, v_0, D, E_{sh}, E_{st}$, and ζ , are constant in space and time, following the assumptions from the Taylor expansion in (4). Similar idealized flow structures were illustrated in Petterssen (1936; 1940, chapter 5; 1956, section 2.7). Figure 1a shows the above flow field with a pure uniform deformation E : $E_{st} = E$ ($u_0 = v_0 = E_{sh} = D = \zeta = 0$).

The frontogenetic aspects of this flow were first discussed by Bergeron (1928). Both the instantaneous dilatation and contraction rates are uniform over the domain and are equal to $E/2$ by (10a) and (10b), respectively. Because of the linear nature of the flow in (13a) and (13b), ψ_d and ψ_c have the same orientation at every point in the flow, although this is not the case in nonlinear flows. The axes of dilatation and contraction are always perpendicular to each other in this, and every, flow (e.g., Fig. 1). When divergence equal and opposite to the deformation is added to the flow (Fig. 1b), $c = E$ and $d = 0$, such that the flow is characterized by pure contraction and no dilatation. The airstream boundaries in the two flows in Fig. 1 are oriented east–west, parallel to the axis of dilatation.

b. Relationship to accumulation and the vector frontogenesis function

Because σ and ω reflect the instantaneous motion of any parcel pair (i.e., changes in the magnitude and orientation of the corresponding separation vector), the time tendency of conserved passive tracers can be diagnosed using these expressions. For example, given a conserved quantity Q ,

$$|\nabla Q| = \frac{\delta Q}{\delta r},$$

where $\nabla = \mathbf{i} \partial/\partial x + \mathbf{j} \partial/\partial y$, and $\delta r = |\delta \mathbf{r}|$, the distance separating two parcels oriented along the gradient. The time tendency of the magnitude of the gradient can be written

$$\begin{aligned} \frac{d|\nabla Q|}{dt} &= \frac{d}{dt} \left(\frac{\delta Q}{\delta r} \right), \\ \frac{d|\nabla Q|}{dt} &= - \frac{\delta Q}{(\delta r)^2} \frac{d(\delta r)}{dt}. \end{aligned} \quad (14)$$

From (2),

$$\delta r = \delta r(0) \exp(\sigma|_{\phi=\eta+\pi/2} t),$$

or

$$\sigma|_{\phi=\eta+\pi/2} = \frac{1}{\delta r} \frac{d(\delta r)}{dt},$$

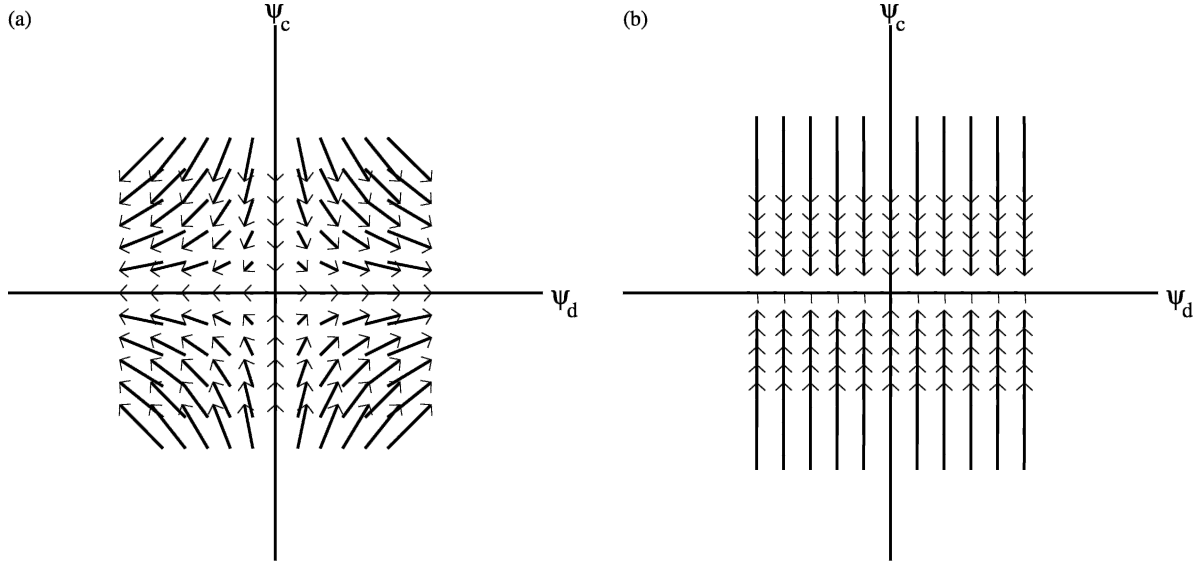


FIG. 1. Idealized wind fields given by (13a) and (13b) in the text. Here, $\zeta = 0$. Solid lines indicate the axes of dilatation (ψ_d) and contraction (ψ_c). (a) Pure stretching deformation: $E_{st} = E$; $u_0 = v_0 = E_{sh} = D = 0$. (b) As in (a), except $D = -E$.

where

$$\eta = \tan^{-1} \left(- \frac{\partial Q / \partial x}{\partial Q / \partial y} \right)$$

is the local orientation of a line of constant Q and is perpendicular to the orientation of the separation vector ϕ (i.e., $\phi = \eta + \pi/2$). This expression for σ represents the linear strain rate in the direction of the gradient. Thus, (14) can be written

$$\frac{d|\nabla Q|}{dt} = -|\nabla Q| \sigma|_{\phi=\eta+\pi/2}$$

Substituting (11a) yields

$$\frac{d|\nabla Q|}{dt} = -\frac{1}{2} |\nabla Q| [E \cos 2(\psi_d - \eta - \pi/2) + D].$$

Defining $\beta = \psi_d - \eta$,

$$\frac{d|\nabla Q|}{dt} = \frac{1}{2} |\nabla Q| (E \cos 2\beta - D). \tag{15}$$

This expression is termed *accumulation* $A(Q)$ (e.g., Saucier 1955, 363–373). For example, if Q is the potential temperature θ , (15) becomes

$$A(\theta) = \frac{d}{dt} |\nabla \theta|,$$

which is equivalent to the Petterssen (1936) frontogenesis function F . As shown by (2.3a) and (2.10a) in Keyser et al. (1988), F is related to expressions for the scalar frontogenesis function F_n of the vector frontogenesis:

$$F_n = -\frac{d}{dt} |\nabla \theta|,$$

$$F_n = -\frac{1}{2} |\nabla \theta| (E \cos 2\beta - D). \tag{16a}$$

Similarly, by multiplying $|\nabla \theta|$ by the rotation rate $\omega|_{\phi=\eta}$ (i.e., the rotation rate valid for a parcel oriented along the isentrope or, more simply, the rotation rate of the isentrope) in (11b), the expression for the rotational component F_s of the vector frontogenesis function, (2.10b) in Keyser et al. (1988), can be derived:

$$F_s = \frac{1}{2} |\nabla \theta| (E \sin 2\beta + \zeta). \tag{16b}$$

As discussed in more detail by Keyser et al. (1988), the expression for F_n is equal and opposite to the Lagrangian frontogenesis function F developed by Petterssen (1936). Equation (16a) expresses the result that, if the angle between the axis of dilatation and the isentrope is less than 45° , deformation is frontogenetical. Convergence is frontogenetical irrespective of the orientation of the isentropes. Diagnosis of F_n for a given flow field indicates the forcing for vertical motion on the frontal scale.

Equation (16b), on the other hand, expresses a measure of the rotation of the isentropes, where positive values of F_s imply cyclonic rotation. For example, if the axis of dilatation is oriented between 0° and 90° counterclockwise of the isentropes, the thermal gradient rotates counterclockwise. In the Northern Hemisphere, cyclonic vorticity results in the counterclockwise rotation of the thermal gradient, whereas anticyclonic vorticity results in the clockwise rotation of the thermal

gradient, both irrespective of the orientation of the isentropes. Diagnosis of F_s for a given flow field indicates the forcing for vertical motion on the scale of the baroclinic wave. Keyser et al. (1988) also showed the relationship between the vector form of the frontogenesis function and the Q vector (Hoskins et al. 1978). Barnes and Colman (1993, 1994), for example, have applied these concepts to observed weather events.

To summarize this section, relationships were developed based on the rate of change of the separation vector, the infinitesimal vector connecting two adjacent air parcels. The instantaneous dilatation and contraction rates d and c were introduced, and their relationship to axes of dilatation and contraction, ψ_d and ψ_c , respectively, were detailed. The maximum and minimum rotation rates for adjacent air parcels, Ω_+ and Ω_- , respectively, were presented. The intimate relationship between the growth rate of the separation vector σ and scalar frontogenesis function F_n , and the rotation rate of the separation vector ω and the rotational component of the vector frontogenesis function F_s , was demonstrated. In addition, all the above expressions are written in terms of Galilean invariant quantities, implying that these expressions are not dependent on a particular reference frame. This framework identifies the strength and orientation of airstream boundaries in flows with deformation and divergence. When vorticity is present, however, more general expressions to diagnose the airstream boundaries may be required. These are developed in the next section.

3. Asymptotic dilatation and contraction rates

Consider the Petterssen (1936) frontogenesis function F . The frontogenesis function quantitatively assesses the instantaneous processes that lead to a changing magnitude of the horizontal potential temperature gradient from the perspective of an air parcel. In other words, the Petterssen (1936) frontogenesis function is a kinematic Lagrangian expression: the existence of a region of positive F does not necessarily imply that a front eventually forms in that area. Because Petterssen (1936) frontogenesis is an instantaneous Lagrangian diagnostic, air parcels must travel within regions of large frontogenesis to experience the prolonged effects of frontogenesis. As noted by Hoskins and West (1979, p. 1674), Hoskins (1982, p. 146), Xu (1988, p. 1234), and Rotunno et al. (1994, p. 3373), the formation of a front occurs where air parcels reside in a region of positive Petterssen (1936) frontogenesis for a sufficiently long time. Doswell (1984) showed that, although vorticity could not contribute directly to Petterssen (1936) frontogenesis, it could rotate the isotherms into a position in the flow that was more favorable frontogenetically.

The diagnostics in the last section are very much analogous to these aspects of frontogenesis. Although ψ_d and ψ_c represent the orientations of maximum

growth and decay, respectively, of the separation vector between adjacent parcels, in general, parcels oriented along these axes experience such rates of growth and decay (d and c , respectively) instantaneously only. These diagnostics cannot express the long-term formation and evolution of airstream boundaries, much as Petterssen (1936) frontogenesis cannot express the long-term formation and evolution of fronts. The goal of this section is to derive expressions to describe the long-term behavior of air-parcel pairs.

Consider a flow with pure deformation (Fig. 1a) or a flow with deformation and divergence (Fig. 1b). As was shown in section 2a, the axis of dilatation and the airstream boundary have the same orientation in such flows. If a parcel pair is oriented along the axis of dilatation, it experiences the largest instantaneous dilatation rate for that location instantaneously. When vorticity is present, however, parcel pairs cannot stay in that orientation, as discussed in regard to (8b); in other words, vorticity rotates the air-parcel pair away from the axis of dilatation. In a similar way, the axis along which the strongest deformation occurs (axis of dilatation) is not the same axis along which the air parcels experience long-term separation. It follows that the axis of dilatation may not be the axis along which the airstream boundary forms, as is shown for fronts in which the axis of dilatation forms an acute angle with the front (Keyser et al. 1988; Bishop 1996; Schultz 2004).

Because rotation is responsible for moving air-parcel pairs out of alignment with the axes of dilatation and contraction, the instantaneous contraction rate reflects a long-term growth rate only if the air-parcel pair is aligned with an axis of zero rotation. Consequently, (8b) is solved when $\omega = 0$:

$$\zeta = \pm E \sin 2(\psi - \chi), \quad (17)$$

where ϕ has been replaced with χ , the orientation of the axis of nonrotation. In order for a unique axis of nonrotation to exist, (17) states that $E \geq |\zeta|$. When $E \geq |\zeta|$, the two solutions to (17) are

$$\chi_d = \psi_d + \frac{1}{2} \sin^{-1} \left(\frac{\zeta}{E} \right), \quad (18a)$$

$$\chi_c = \psi_c - \frac{1}{2} \sin^{-1} \left(\frac{\zeta}{E} \right), \quad (18b)$$

where χ_d and χ_c are called the *asymptotic dilatation axis* and *asymptotic contraction axis*, respectively. These correspond to the *axis of outflow* and *axis of inflow*, respectively, of Petterssen (1936; 1940, 252–256; 1956, p. 38). When $|\zeta| > E$, there is no solution where $\omega = 0$, and no asymptotic dilatation or contraction axes exist. When $\zeta = 0$, $\phi = \chi$, and the axis of dilatation and axis of contraction are equal to the asymptotic dilatation axis and asymptotic contraction axis, respectively (e.g., section 2a).

Equation (17) can be rewritten

$$\cos^2 2(\psi - \chi) = 1 - \frac{\zeta^2}{E^2}. \quad (19)$$

Squaring the expression for the growth rate σ , (11a), and employing (19) yields

$$\sigma|_{\phi=\chi} = \frac{1}{2}[D \pm (E^2 - \zeta^2)^{1/2}]. \quad (20)$$

Because $E \geq |\zeta|$ for an axis of nonrotation to exist, (20) is maximum when the sign following D is positive and is minimum when the sign is negative. Consequently, χ_d and χ_c are defined such that $\sigma|_{\phi=\chi_d} \geq \sigma|_{\phi=\chi_c}$.

Defining the *asymptotic dilatation rate* (\mathcal{D}) and the *asymptotic contraction rate* (\mathcal{C}) to be the growth rate along $\phi = \chi_d$ and the negative of the decay rate along $\phi = \chi_c$, respectively,

$$\mathcal{D} = \sigma|_{\phi=\chi_d} = \frac{1}{2}[D + (E^2 - \zeta^2)^{1/2}], \quad (21a)$$

$$\mathcal{C} = -\sigma|_{\phi=\chi_c} = \frac{1}{2}[-D + (E^2 - \zeta^2)^{1/2}]. \quad (21b)$$

The asymptotic dilatation rate, \mathcal{D} , represents the long-term rate at which the distance between two adjacent parcels increases for steady-state wind fields that vary linearly with the spatial coordinates. Conversely, the asymptotic contraction rate, \mathcal{C} , represents the long-term rate at which the distance between two adjacent parcels decreases, given the same conditions. We use the term *asymptotic* to describe these diagnostics because asymptotic implies long-term behavior given enough time. What constitutes “long term” is a length of time during which the steady-state (or slowly varying) and Taylor-expansion approximations made earlier in this paper are valid. Analogous to frontogenesis, these diagnostics represent locations where the flow is acting to create airstream boundaries instantaneously. If the flow is steady and the wind field varies linearly in space, the asymptotic dilatation axis is the eventual location of the airstream boundary.

Even though we use the adjective asymptotic to represent the long-term behavior of the air-parcel pairs, it is important to highlight that these diagnostics are computed kinematically from instantaneous fields. Although these expressions are exact instantaneously, they are only estimates of the long-term behavior of time-varying flow, as shown later in the paper for an idealized flow. Application of these diagnostics to real nonsteady atmospheric flows is the subject of future research.

These expressions are similar to those for the instantaneous rates d and c , (10a) and (10b), respectively, except for the addition of the vorticity ζ in (21a) and (21b). Therefore, by including the effect of vorticity, the expressions for the instantaneous dilatation and contraction rates become expressions for the asymptotic dilatation and contraction rates, respectively.

Finally, the orientation of χ_c is aligned along the direction in which the separation vector experiences its most rapid rate of contraction in the longer term, much as ψ_c represents the directions in which the separation vector experiences its most rapid rate of decrease instantaneously. Thus, if an airstream boundary were to form, χ_d represents its likely orientation, given the assumptions about steady, linear flow. Because such long-term or time-averaged contraction rates are related to airstream boundaries (section 1), the asymptotic dilatation axis and asymptotic contraction rate are proposed to be better measures of the development of airstream boundaries than the axis of dilatation and instantaneous contraction rate. This statement is reminiscent of that in Petterssen (1940, p. 255): “the axis of outflow [asymptotic axis of dilatation] is not a creator of fronts but a collector of fronts; for though frontogenesis may occur anywhere in the field, the line of frontogenesis will move toward this axis, and the resulting front will be found at this axis, or close to it” (Petterssen’s emphasis).

a. Examples

Because the flow in Fig. 1 possessed no vorticity, by (18a) and (18b), asymptotic axes of dilatation and contraction align along the axes of dilatation and contraction, respectively. Thus, the airstream boundary occurs where the axis of dilatation occurs.

Next, consider the flow fields shown in Fig. 2, the same as those in Fig. 1 except for the addition of vorticity ($\zeta = 0.6E$). Whereas parcel pairs oriented along the axes of dilatation and contraction (ψ_d and ψ_c) in Fig. 1 would remain oriented along those axes, in Fig. 2 parcel pairs oriented along the axes of dilatation and contraction would rotate away from those axes and eventually reach the asymptotic dilatation axis (χ_d). Clearly, the airstream boundaries lie along the asymptotic axes of dilatation in these two flows. Adding a constant uniform flow to these flow fields would eliminate the col point at the origin where the wind speed is zero, but the asymptotic dilatation and contraction axes, as well as the axes of dilatation and contraction, would remain unchanged. Thus, in these two flows, although the maximum instantaneous dilatation rate occurs along the axes of dilatation (ψ_d), the airstream boundaries occur along the asymptotic axes of dilatation (χ_d). The effect of the vorticity ($\zeta = 0.6E$) is to rotate the asymptotic axis of dilatation about 18° counterclockwise from the axis of dilatation and to rotate the asymptotic axis of contraction about 18° clockwise from the axis of contraction.

Unlike the axes of dilatation and contraction, χ_d and χ_c need not be orthogonal (e.g., Fig. 2). Indeed, the angle between χ_d and χ_c is zero when the magnitude of the vorticity equals the deformation, as per (18a) and (18b) (e.g., Fig. 3, which is the same as Fig. 1 except that $\zeta = E$). In this case (Fig. 3), the flow is sheared across a northeast–southwest-oriented shear line. Since $\chi_d =$

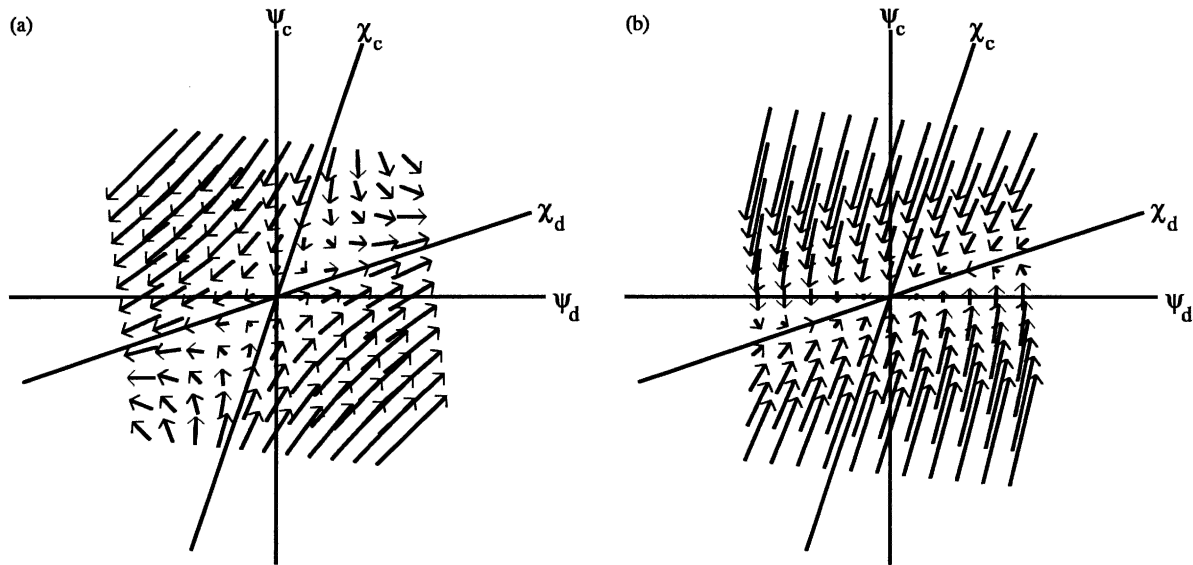


FIG. 2. As in Fig. 1, except $\zeta = 0.6E$, and solid lines indicate the asymptotic dilatation axis (χ_d) and asymptotic contraction axis (χ_c).

$\psi_d + (\pi/4)$ by (18a) in this flow, ψ_d is oriented east-west, although the position of the airstream boundary (χ_d) is oriented northeast-southwest, an orientation rotated 45° cyclonically from the axis of dilatation.

This result is consistent with that of Keyser et al. (1988), Bishop (1996), and Schultz (2004) who showed that fronts with vorticity do not align along the axis of dilatation, but at some angle cyclonically rotated from the axis of dilatation. In such a case, the deformation along the front acting to rotate the isentropes anticyclonically offsets the vorticity along the front acting to rotate the isentropes cyclonically, as described by (18a).

These competing effects are demonstrated in the idealized shear flow in Keyser et al. (1988, their Figs. 5 and 6), where the vorticity equals the deformation along the shear line ($x = 0$), producing the axes of dilatation 45° anticyclonically to the shear line.

When the magnitude of the vorticity is greater than the deformation, no axes of zero rotation exist (e.g., Fig. 4, which is the same as Fig. 1 except that $\zeta = 1.2E$). In such a situation, when the flow is nondivergent, the fluid is trapped (e.g., Fig. 4a). When the flow possesses divergence, parcel pairs will spiral around and approach each other when $D < 0$ (e.g., Fig. 4b) or spiral

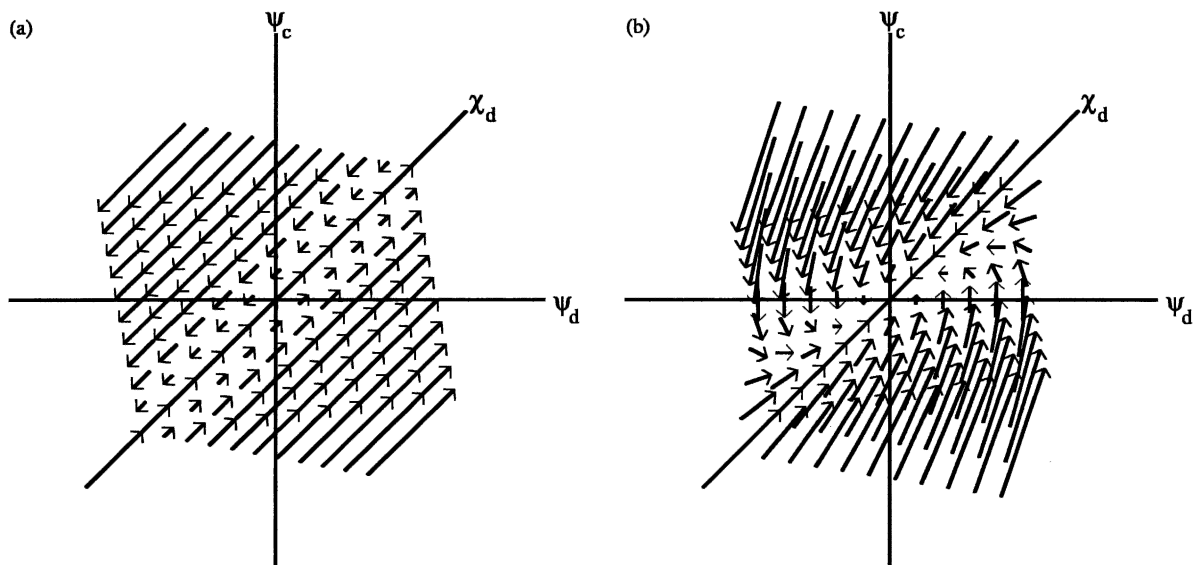
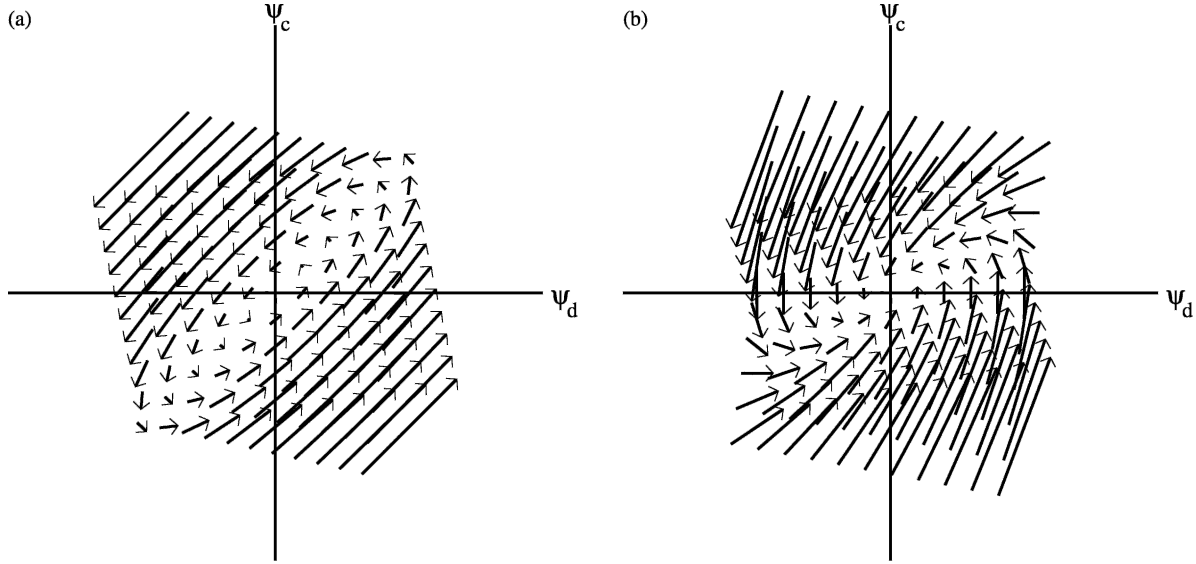


FIG. 3. As in Fig. 1, except $\zeta = E$, and solid lines indicate the asymptotic dilatation axis (χ_d).

FIG. 4. As in Fig. 1, except $\zeta = 1.2E$.

around and separate from each other when $D > 0$ (e.g., Petterssen 1956, his Fig. 2.7.2F). The dynamics of parcels in this context have been discussed previously (e.g., McWilliams 1984; Benzi et al. 1988; Pierrehumbert and Yang 1993; Cunningham and Keyser 2000, 2004).

*b. Development of the fluid-trapping diagnostic:
Relationship to the Lyapunov exponent*

The expressions for \mathcal{D} in (21a) and C in (21b) represent the long-term rate at which the distance between two adjacent parcels increases or decreases, respectively. Depending on the value of \mathcal{D} and the sign of $E^2 - \zeta^2$, however, C may be purely real, purely imaginary, or complex.

If the flow is nondivergent, the interpretation can be simplified. In this case, $\mathcal{D} = C$, implying that the rate at which adjacent air parcels approach each other along the asymptotic contraction axis is the same rate at which air parcels separate along the asymptotic dilatation axis, as would be expected in nondivergent flow. (Because $\mathcal{D} = C$, we choose C to represent the growth rate of an airstream boundary to maintain consistency with C and c from earlier in this paper.) In nondivergent flow, C is either real and nonnegative when $E^2 - \zeta^2 \geq 0$ or is purely imaginary when $E^2 - \zeta^2 < 0$. If C is real and nonnegative, then adjacent parcels separate from each other (e.g., Figs. 2a and 3a). If C is purely imaginary (e.g., Fig. 4a), these parcels are isolated from the surrounding flow (i.e., trapped). Therefore, C can be used to describe the behavior of air-parcel pairs in time and is dependent on the sign of $E^2 - \zeta^2$.

Note that \mathcal{D}^2 and C^2 , if nondivergent, are equal to the product of Ω_+ and Ω_- , what we term Ω^2 , the *fluid-trapping diagnostic*:

$$\Omega^2 = \Omega_+ \Omega_- = \frac{1}{4}(E^2 - \zeta^2). \quad (22)$$

[As an aside, Petterssen (1953), Xu (1990, 1992), and Cunningham and Keyser (2000, 2004) showed that Ω^2 is proportional to the square of the ageostrophic vorticity (Q in Cunningham and Keyser 2000).]

A similar result was discussed by McWilliams (1984) for a two-dimensional idealized simulation of turbulent equivalent-barotropic flow and Pierrehumbert and Yang (1993) for a passive tracer being advected on a two-dimensional, nondivergent, isentropic surface. Benzi et al. (1988), Schubert et al. (1999), and Cunningham and Keyser (2000, 2004) also derived similar expressions. As these studies noted, the relative magnitudes of deformation and vorticity (or, equivalently, the sign of $E^2 - \zeta^2$) can be used to distinguish between so-called straining or turbulent regions of the fluid dominated by deformation ($E > |\zeta|$) and so-called eddy or neutral regions of the fluid dominated by vorticity ($|\zeta| > E$). This analysis can be extended to flows with divergence, such that the eddy region will expand in divergent flow and contract in convergent flow.

As shown in appendix B, expressions for \mathcal{D} and C can also be derived from calculating the two eigenvalues of the flow, λ_1 and λ_2 , where the separation vector can be expressed as a linear combination of two eigenvectors:

$$\delta \mathbf{r} = \mathbf{A}e^{\lambda_1 t} + \mathbf{B}e^{\lambda_2 t}. \quad (23)$$

Written in this form, the eigenvectors point along χ_d and χ_c , the axes where $\omega = 0$. When either \mathbf{A} or \mathbf{B} is zero, the separation vector is constrained to move along one eigenvector direction. This is equivalent to restricting ω to be zero, implying that $\lambda = \sigma|_{\phi=\chi}$. For nondivergent flow, the eigenvalue associated with the asymptotic dilatation rate \mathcal{D} is positive, and the eigenvalue associated with the asymptotic contraction rate C is negative. At large t , the term in (23) with the positive eigenvalue dominates, and thus, only one eigenvalue is

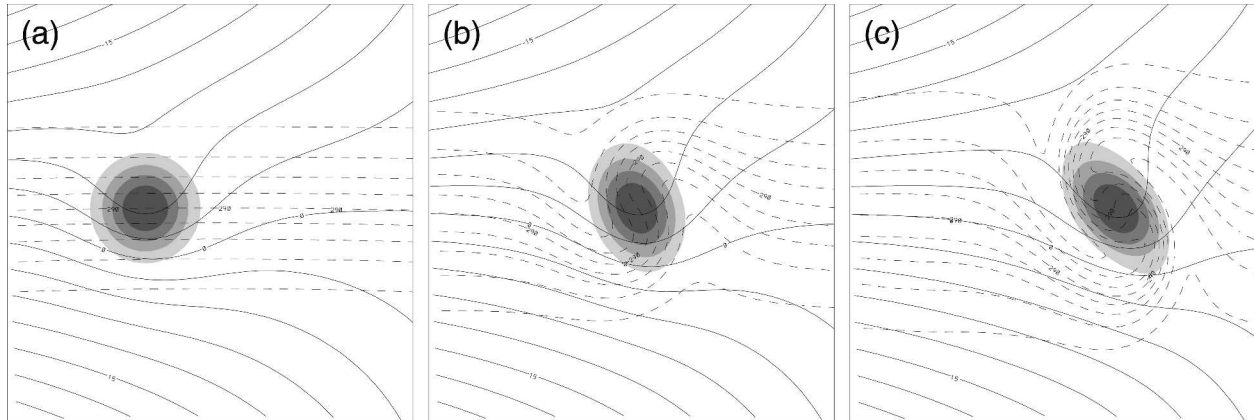


FIG. 5. Evolution of Doswell vortex in diffluent background flow at (a) 0, (b) 12, and (c) 24 h. Potential temperature (dashed lines every 2 K), streamfunction (solid lines every $3 \times 10^6 \text{ m}^2 \text{ s}^{-1}$), and relative vorticity (shaded for values greater than $2 \times 10^{-5} \text{ s}^{-1}$, in increments of $2 \times 10^{-5} \text{ s}^{-1}$).

needed. The single eigenvalue at large t is called the *Lyapunov exponent*.

In studies of chaotic mixing of geophysical fluids (e.g., Pierrehumbert and Yang 1993; references in Zeng et al. 1993), the Lyapunov exponent is used as a measure of the maximum uncertainty of a parcel's future position as a function of the uncertainty in its initial position. The Lyapunov exponent λ represents the maximum growth rate of parcel-pair separations averaged over the fluid. Thus, there is some similarity between the Lyapunov exponent and our diagnostic \mathcal{D} , where λ is long term and \mathcal{D} is instantaneous, and where λ is averaged over the entire flow and \mathcal{D} is local. Thus, we can say \mathcal{D} represents the *instantaneous local Lyapunov exponent*, which is dependent on both time and position.

The use of the instantaneous local Lyapunov exponent to investigate the stretching of fluid elements is not new. For example, similar expressions have been developed previously by Batchelor (1952), Vuorela (1953), and Welander (1955). The instantaneous local Lyapunov exponent is also related to the efficiency factor used in studies of mixing, such as Fairlie et al. (1999), where the efficiency factor is equivalent to the square of the instantaneous local Lyapunov exponent. Thus, the asymptotic dilatation rate \mathcal{D} , or equivalently the instantaneous local Lyapunov exponent, helps to bridge the gap between the kinematic framework posed by synoptic meteorology and the theoretical framework of turbulent mixing.

To summarize this section, we showed that flows with vorticity would possess airstream boundaries differing in orientation from the axis of dilatation, if $E \geq |\zeta|$. Expressions for the asymptotic dilatation and contraction axes were derived and the asymptotic dilatation axis was proposed to represent the location of the airstream boundary better than the axis of dilatation. The asymptotic dilatation rate is also related to the instantaneous local Lyapunov exponent and a fluid-trapping

diagnostic that can be used to assess where the flow is characterized by eddies (e.g., trapped flow). Finally, in this section, these diagnostics were applied to steady, idealized, linear flows. Applying these diagnostics to a nonsteady, idealized, nonlinear flow is the subject of the next section.

4. Application to an ideal cyclone

To illustrate the application of these diagnostic expressions from sections 2 and 3 to an idealized atmospheric flow, we choose a synoptic-scale flow pattern featuring both deformation and vorticity. We choose a nondivergent framework in which to illustrate these diagnostic expressions to simplify the interpretation. Nevertheless, these results could be generalized to more complex flows using the full divergent formulation in this paper. Even in such a nondivergent flow, contraction between air-parcel pairs occurs and airstream boundaries form. After a brief description of the model, two aspects of the flow are examined: the evolution of parcel pairs in section 4a and the airstream boundaries in section 4b.

We construct an idealized synoptic-scale flow pattern representing an extratropical cyclone in a diffluent background flow by embedding an idealized Doswell (1984) vortex [also discussed by Davies-Jones (1985) and Doswell (1985)] in nondivergent, diffluent flow as discussed in Schultz et al. (1998). This flow pattern is placed in a time-dependent, nondivergent barotropic model on an f plane, adapted from that of Smith et al. (1990). Details of the barotropic model and experimental setup can be found in section 4 of Schultz et al. (1998). Except for weak numerical diffusion, potential temperature is a conserved passive tracer in this model.

The evolution of the cyclone and potential temperature field is shown in Fig. 5 of this paper and in Fig. 13 of Schultz et al. (1998). At the initial time, the flow field

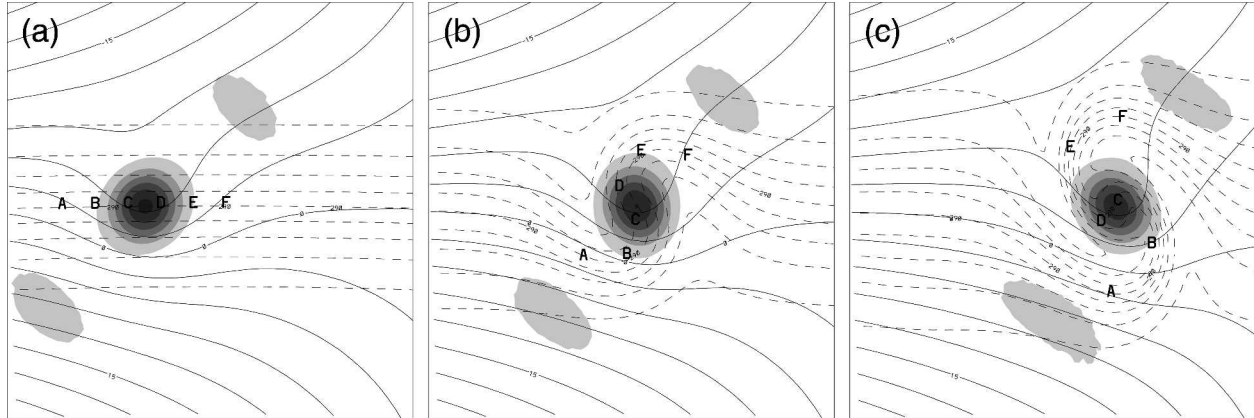


FIG. 6. Evolution of Doswell vortex in diffluent background flow at (a) 0, (b) 12, and (c) 24 h. Potential temperature (dashed lines every 2 K), streamfunction (solid lines every $3 \times 10^6 \text{ m}^2 \text{ s}^{-1}$), and fluid-trapping diagnostic Ω^2 (shaded for negative values, in increments of $5 \times 10^{-10} \text{ s}^{-2}$). Letters A–F represent fluid parcels as discussed in the text.

acts on a potential temperature gradient oriented to the south (i.e., isotherms are oriented east–west), and the relative vorticity of the total horizontal wind is circularly shaped (Fig. 5a). Twelve hours later (Fig. 5b), the isentropes are rotated cyclonically by the vorticity. In addition, both the isentropes and the relative vorticity maximum are stretched by the background deformation field (Fig. 5b). At 24 h, the isentropes continue to be wrapped cyclonically around the cyclone (Fig. 5c), analogous to the occlusion process in the Norwegian cyclone model (e.g., Bjerknes and Solberg 1922).

a. Evolution of parcel pairs

To examine the fluid-trapping properties of the flow, we apply the diagnostic C . Because the flow is nondivergent, we look for negative values of Ω^2 where adjacent fluid parcels are trapped. Regions of trapped fluid are found near the center of the cyclone and in two regions northeast and southwest of the cyclone (Fig. 6). Unlike the relative vorticity (Fig. 5), the region of negative Ω^2 values near the cyclone center is not stretched as much by the deformation field. Thus, care should be taken in trying to relate fluid trapping to the location of the vorticity maximum, as sometimes happens when viewing water-vapor satellite imagery of a drier region commonly attributed to previously descended air associated with a short-wave trough. For an example of such a dry region associated with a short-wave trough, see Muller and Fuelberg (1990).

To confirm the fluid trapping, sample trajectories of parcel pairs inside and outside of the region of negative Ω^2 near the cyclone center are computed and displayed in Fig. 6. Unlike parcel pairs outside this region (e.g., A/B and E/F), parcel pairs inside this region do not separate, but are trapped in this two-dimensional flow (e.g., C/D). Thus, the parcels near the cyclone center in the region of negative Ω^2 are isolated from the surrounding flow.

Outside the region of negative Ω^2 near the center of the cyclone, deformation is greater than the magnitude of the vorticity and parcel pairs separate along the asymptotic dilatation axis, χ_d (Fig. 7). For example, parcels I and J are initially located in a region of large asymptotic contraction rate and their separation vector $\delta \mathbf{r}$ is oriented parallel to the asymptotic dilatation axis (Fig. 7a). Consequently, the magnitude of $\delta \mathbf{r}$ for I/J increases by 12 and 24 h (Figs. 7b,c). In contrast, parcels G and H are located in the same region of large asymptotic contraction rate but their separation vector $\delta \mathbf{r}$ is oriented nearly perpendicular to the asymptotic dilatation axis (Fig. 7a). In this case, the magnitude of $\delta \mathbf{r}$ between G and H (i.e., their separation) decreases (Fig. 7b).

By 12 h, the separation vector for parcels G and H rotates and becomes oriented nearly parallel to the asymptotic dilatation axis (Fig. 7b). Thus, like parcel pair I/J, G/H finds itself in an orientation such that these parcels, too, separate by 24 h (Fig. 7c). In general, two parcels in a region of large asymptotic contraction rate inevitably separate as they rotate to become parallel to the asymptotic dilatation axis. Near the center of the cyclone, $\Omega^2 < 0$, so no axis of nonrotation (χ_d) exists, as air parcels in this region are trapped (e.g., Fig. 6).

b. Airstream boundaries

As discussed in section 1, the average contraction rate C can be used as a measure of the strength of an airstream boundary for flows. The 12-h average contraction rate ending at 24 h computed for the ideal cyclone shows the largest values located within two north–south-oriented regions southeast and northwest of the cyclone center (Fig. 8a). [Because of the scale-contracting effect of divergence, the regions of large 12-h average contraction rates for this nondivergent flow are broader than they would be in the atmosphere for a rapidly developing cyclone, such as the one inves-

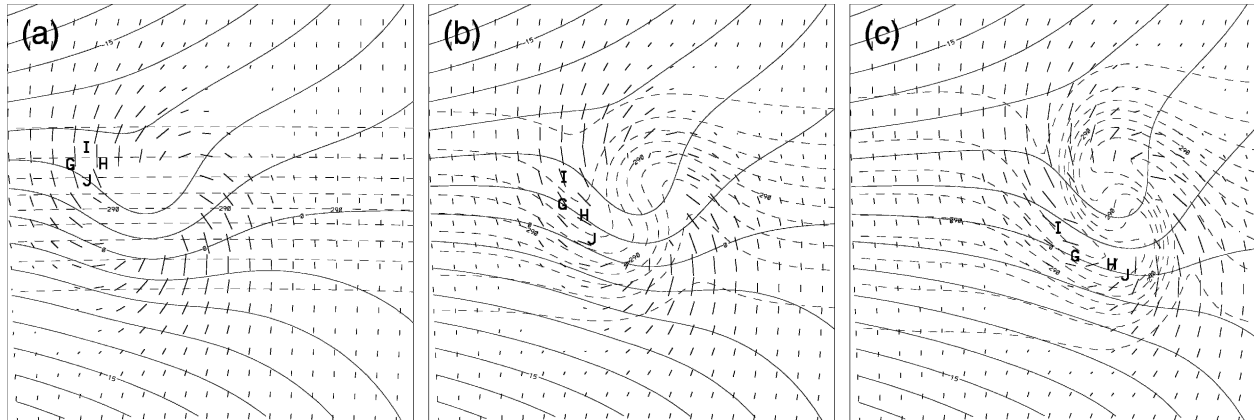


FIG. 7. Evolution of Doswell vortex in diffluent background flow at (a) 0, (b) 12, and (c) 24 h. Potential temperature (dashed lines every 2 K), streamfunction (solid lines every $3 \times 10^6 \text{ m}^2 \text{ s}^{-1}$), and asymptotic dilatation axes (length proportional to the asymptotic contraction rate C and orientation parallel to χ_d). Letters G–J represent fluid parcels as discussed in the text.

tigated in Cohen and Kreitzberg (1997).] The similarity between the largest 12-h average contraction rates and the strengthening fronts is characteristic of the airstream boundary separating the warm and cold air masses (Fig. 8a).

As discussed in section 3, the asymptotic contraction rate is expected to be more closely related to the strength of airstream boundaries than the instantaneous contraction rate. Figures 8a and 8b show the strong similarity between C and the asymptotic contraction rate, especially outside the cyclone center, supporting our expectation. A comparison between the asymptotic and instantaneous contraction rates and axes shows that, outside of the cyclone center, the two are also very similar in magnitude and in orientation (cf. Figs. 8b and 8c). Although the orientations of the axes of dilatation and asymptotic dilatation axes are similar

for this idealized cyclone, Figs. 2 and 3 show these axes can be dramatically different in other flow patterns.

Near the cyclone center where air parcels are trapped (e.g., Fig. 6), the differences are quite substantial. Whereas the asymptotic contraction rate is imaginary, the instantaneous contraction rate is positive and large (cf. Figs. 8b and 8c). The strong shear in the center of the vortex implies a large instantaneous dilatation rate where parcels are separating at an instant, as in Fig. 4, but the parcels are ultimately trapped, so the asymptotic contraction rate is imaginary.

As mentioned earlier, both the instantaneous contraction rate and asymptotic contraction rate potentially represent instantaneous measures of airstream boundaries. Even with positive c and C , the airstream boundary may be weakening or strengthening depending on whether the value is less than or greater than the

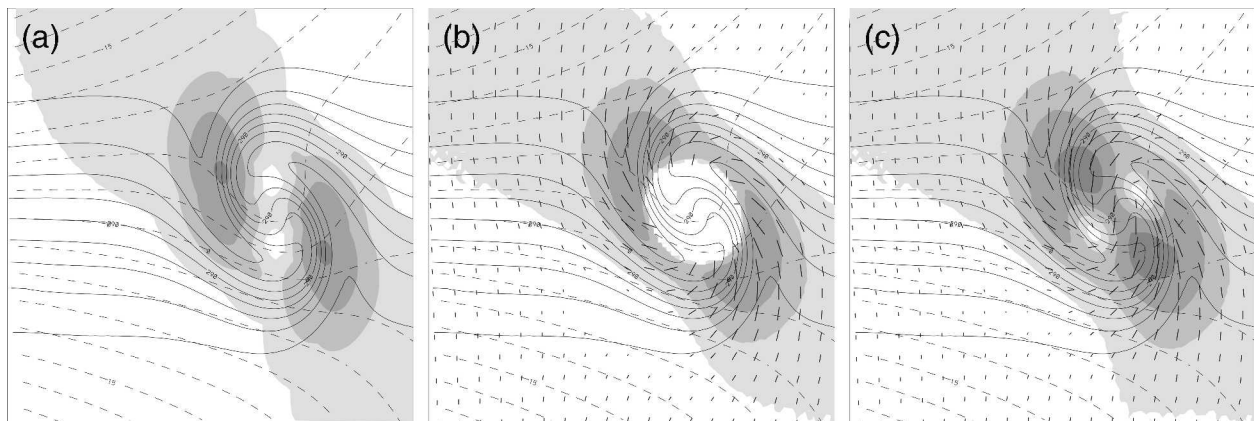


FIG. 8. Doswell vortex in diffluent background flow at 24 h. Potential temperature (solid lines every 2 K) and streamfunction (dashed lines every $3 \times 10^6 \text{ m}^2 \text{ s}^{-1}$). (a) The 12-h average contraction rate C (shaded greater than $0.5 \times 10^{-1} \text{ s}^{-1}$, in increments of $0.5 \times 10^{-1} \text{ s}^{-1}$). (b) Asymptotic contraction rate C (shaded greater than $0.5 \times 10^{-1} \text{ s}^{-1}$, in increments of $0.5 \times 10^{-1} \text{ s}^{-1}$) and asymptotic dilatation axes (length proportional to the asymptotic contraction rate C and orientation parallel to χ_d). (c) Instantaneous contraction rate c (shaded greater than $0.5 \times 10^{-1} \text{ s}^{-1}$, in increments of $0.5 \times 10^{-1} \text{ s}^{-1}$) and axes of dilatation (length proportional to the instantaneous contraction rate c and orientation parallel to ψ_d).

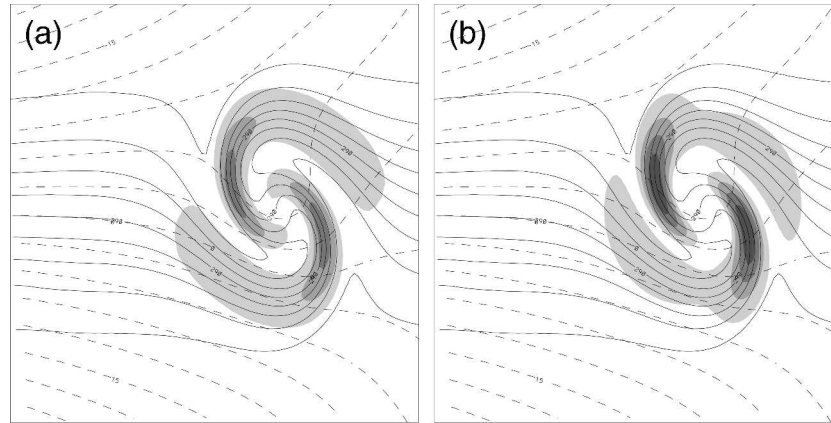


FIG. 9. Doswell vortex in diffluent background flow at 24 h. Potential temperature (solid lines every 2 K) and streamfunction (dashed lines every $3 \times 10^6 \text{ m}^2 \text{ s}^{-1}$). (a) Potential temperature gradient [shaded greater than $2 \text{ K (100 km)}^{-1}$, in increments of $2 \text{ K (100 km)}^{-1}$]. (b) The 12-h Lagrangian-averaged frontogenesis at the ending points of the trajectories [shaded greater than $0.1 \text{ K (100 km)}^{-1} (3 \text{ h})^{-1}$, in increments of $0.2 \text{ K (100 km)}^{-1} (3 \text{ h})^{-1}$].

average rate C . As such, it would be illuminating to compare the history of the instantaneous and asymptotic rates and see the relationship between the strength and position of the 12-h airstream boundary and the diagnostic quantities. To do this, the instantaneous and asymptotic contraction rates are averaged along the paths of the parcel trajectories. (Because the asymptotic contraction rate is only exact if the flow is steady and the gradients are constant in space, such a Lagrangian-averaged asymptotic contraction rate is one attempt to measure the real long-term separation rate.)

Before performing such a Lagrangian average, we first show what the calculation looks like for a field easier to interpret: potential temperature. In Fig. 9a, regions of large $\nabla\theta$ are shaded, indicating the regions of large potential temperature gradients at 24 h. In Fig. 9b, the instantaneous values of frontogenesis have been determined along the parcel trajectories over the previous 12 h, and an average rate of frontogenesis is shaded at the ending points of the trajectories. Where the Lagrangian-average frontogenesis is large, the potential temperature gradient is also large (cf. Figs. 9a and 9b). Unfortunately, a perfect match is not possible, because the average frontogenesis represents the average change in potential temperature gradient and the initial potential temperature gradient was not uniform throughout the domain. Nevertheless, the similarity in these fields should illustrate the meaning of the Lagrangian average. Such an interpretation of frontogenesis is consistent with the idea that the strongest fronts occur where the forcing for frontogenesis is strong and where air parcels reside in regions of frontogenesis for a long time (e.g., Hoskins and West 1979; Hoskins 1982; Xu 1988; Rotunno et al. 1994).

Returning to the contraction rates, we wish to compare the 12-h average airstream boundaries computed

by the Cohen and Kreitzberg (1997) method (Fig. 10a) with the 12-h Lagrangian-average asymptotic contraction rate (Fig. 10b) and the 12-h Lagrangian-average instantaneous contraction rate (Fig. 10c). Whereas Figs. 10b and 10c are very similar, there are some slight differences within the vortex. In particular, the former more accurately reproduces the strength of the airstream boundaries within the vortex, supporting our contention that the asymptotic contraction rate more accurately reflects the longer-term evolution of air-parcel pairs.

The match is not perfect, however. Within the vortex, there appears to be a weak airstream boundary collocated with the center of the vortex (Fig. 10a), a feature also seen in the integrated instantaneous contraction rates (Fig. 10c). This feature is attributed to enhanced deformation in that area, leading to periodic stretching and compression of the air-parcel pairs as they revolve around each other. Extending the integration to longer time scales removes this feature (not shown).

Whether this pattern holds in real storms remains a subject for future research. However, there is at least one flow structure for which airstream boundaries may be best reflected in the instantaneous contraction rate: cases of pure shear (e.g., Fig. 3a). In these cases, a boundary is still apparent (indicated by the axis marked χ_d in Fig. 3a) and parcels on opposite sides of the boundary move apart with time. However, since $D = 0$ and $\zeta = E$, the asymptotic contraction rate C is zero. This is because the separation of parcel pairs straddling the boundary grows linearly with time rather than exponentially. The orientation of the boundary still mirrors the asymptotic dilatation axis (as opposed to the axis of dilatation), but, in such cases, the instantaneous contraction rate might better reflect the strength of the airstream boundary.

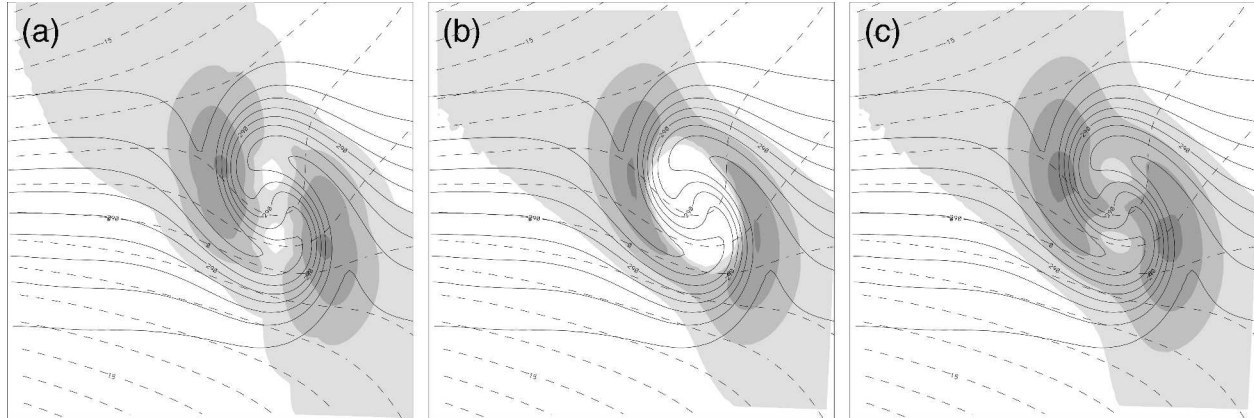


FIG. 10. Doswell vortex in diffluent background flow at 24 h. Potential temperature (solid lines every 2 K) and streamfunction (dashed lines every $3 \times 10^6 \text{ m}^2 \text{ s}^{-1}$). (a) The 12-h average contraction rate C (shaded greater than $0.5 \times 10^{-1} \text{ s}^{-1}$, in increments of $0.5 \times 10^{-1} \text{ s}^{-1}$). (b) The 12-h Lagrangian-averaged asymptotic contraction rate (shaded greater than $0.5 \times 10^{-1} \text{ s}^{-1}$, in increments of $0.5 \times 10^{-1} \text{ s}^{-1}$). (c) The 12-h Lagrangian-averaged instantaneous contraction rate (shaded greater than $0.5 \times 10^{-1} \text{ s}^{-1}$, in increments of $0.5 \times 10^{-1} \text{ s}^{-1}$).

5. Concluding discussion

Owing to gradients of temperature and momentum in the atmosphere, sharp boundaries in temperature and wind develop, known as fronts and airstream boundaries, respectively. Although a diagnostic framework for interpreting fronts has existed for some time, less attention has been devoted to a similar framework for boundaries in the wind field. In our attempt to form such a framework, we unite previously disparate topics such as the frontogenesis function (Petterssen 1936; Keyser et al. 1988), average contraction rate (Cohen and Kreitzberg 1997), axis of outflow (Petterssen 1940, 252–256; 1956, p. 38), and Lyapunov exponent (Zeng et al. 1993).

The principal components of this framework include the following elements:

- 1) Expressions for the separation rate σ and rotation rate ω of two adjacent fluid parcels are derived. At any given time in the fluid, the axis of dilatation ψ_d is the direction along which the separation rate is greatest (the instantaneous dilatation rate d) and is perpendicular to the axis of contraction ψ_c , where the rate of approach is greatest (the instantaneous contraction rate c).
- 2) These expressions for separation and rotation rates are similar to those for the vector frontogenesis function (Keyser et al. 1988), in that the separation rate is related to the scalar frontogenesis (F_n) and the rotation rate is related to the rotational frontogenesis (F_s).
- 3) The asymptotic dilatation and contraction rates \mathcal{D} and C represent the local long-term rates at which two adjacent air parcels separate and approach, respectively, along the axes of nonrotation, also known as the asymptotic dilatation axis χ_d and asymptotic contraction axis χ_c , respectively.

- 4) The instantaneous local Lyapunov exponent, a diagnostic from chaotic mixing studies, is equivalent to the asymptotic dilatation rate \mathcal{D} and, in nondivergent flow, the square root of Ω^2 , the product of the maximum and minimum local rotation rates. These diagnostics can be used to distinguish among parcel pairs being pulled apart, being pushed together, or trapped together in an eddy.

These diagnostics were applied to an idealized cyclone in a nondivergent, barotropic model to identify regions of trapped fluid and to quantitatively diagnose the growth and rotation of the separation vector associated with parcel pairs along airstream boundaries. In addition, because the asymptotic dilatation rate is equivalent to the instantaneous local Lyapunov exponent, the diagnostics can also be applied to predictability studies in order to determine the rate at which air-parcel trajectories would instantaneously diverge from each other.

Although the example presented in section 4 was for a nondivergent idealized flow, these results could be extended for divergent flows. The inclusion of divergence would only modify the essential aspects presented in this paper rather than present dramatically different results, especially for large-scale flows in which divergence tends to be small relative to vorticity and deformation.

This work has three additional implications that are not explored here. First, the distribution of instantaneous local Lyapunov exponent provides information about the power spectra and turbulent mixing within flows such as the atmosphere (e.g., Pierrehumbert and Yang 1993; Schubert et al. 1999). Second, these diagnostics can be used to explore the difference in the location and strength of gradients of a passive tracer and gradients in a buoyancy field (like temperature).

As discussed by MacVean and Woods (1980) and Parker (1999), there can be substantial differences between these two for certain flow fields. Third, although the fluid-trapping diagnostic is strictly only applicable in two-dimensional flow, it can be employed on a nearly conserved surface in three dimensions (e.g., potential vorticity, potential temperature) to illustrate the three-dimensional trapping effects of eddies in geophysical fluids.

Finally, these diagnostics provide new opportunities to diagnose airstream boundaries and fluid trapping in weather phenomena at a variety of scales from mesocyclones in supercell thunderstorms to extratropical cyclones. The application of these diagnostics to nonidealized, observed flow fields in the atmosphere remains a topic for future research.

Acknowledgments. We are deeply indebted to the following individuals and groups for their contributions to this work: the late Prof. Carl Kreitzberg for suggesting that this work be initiated and his guidance; Daniel Keyser for his unwavering encouragement; Robert Davies-Jones and David Larrabee for their assistance with some aspects of our derivation; Charles Doswell for his stimulating discussions on kinematics and frontal structure; Greg Hakim, Doug Lilly, John Locatelli, David Stensrud, and Qin Xu for their comments on earlier versions of this manuscript; Juan Carlos Jusem, Daniel Keyser, Michael Reeder, and Alan Shapiro for their formal and informal reviews, and the Academic Computing Department at East Stroudsburg University and Instrument Specialties Inc. for supplying computer hardware to the first author. Implementation of the simulation and graphics routines used in this research by the first author was supported by Grant 110107-126 from the Faculty Professional Development Council of the State System of Higher Education in Pennsylvania. Some of this research was conducted while the second author was a National Research Council Postdoctoral Research Associate at the National Severe Storms Laboratory (1996–98). Since then, funding for Schultz was provided by NOAA/OAR/NSSL under NOAA–OU Cooperative Agreement NA17RJ1227.

APPENDIX A

List of Symbols

A, B	Eigenvectors
$A(Q)$	Accumulation of passive tracer Q (Saucier 1955, 363–373)
c	Instantaneous contraction rate, $-\sigma _{\phi=\psi_c}$
C	Average contraction rate (following Cohen and Kreitzberg 1997)
C	Asymptotic contraction rate, $-\sigma _{\phi=\chi_c}$
d	Instantaneous dilatation rate, $\sigma _{\phi=\psi_d}$

D	Divergence ($\partial u/\partial x + \partial v/\partial y$)
\mathcal{D}	Asymptotic dilatation rate, $\sigma _{\phi=\chi_d}$; also the instantaneous local Lyapunov exponent
E	Resultant deformation ($E_{st}^2 + E_{sh}^2$) ^{1/2}
E_{sh}	Shearing deformation ($\partial u/\partial y + \partial v/\partial x$)
E_{st}	Stretching deformation ($\partial u/\partial x - \partial v/\partial y$)
f	Coriolis parameter
F	Petterssen (1936) frontogenesis function
F_n	Scalar frontogenesis of the vector frontogenesis function (Keyser et al. 1988)
F_s	Rotational component of the vector frontogenesis function (Keyser et al. 1988)
Q	Passive tracer
r	Distance between parcel pair (separation)
t	Time
u	Eastward velocity component
v	Northward velocity component
u_0, v_0	Constant translation velocity components
x	Eastward displacement component
y	Northward displacement component
β	Angular difference between axis of dilatation (ψ_d) and line of constant Q (η)
$\delta\mathbf{r}$	Infinitesimal separation vector
δr	Magnitude of infinitesimal separation vector ($ \delta\mathbf{r} $)
σ	Growth rate of separation vector
ζ	Relative vorticity ($\partial v/\partial x - \partial u/\partial y$)
η	Local orientation of a line of constant Q
θ	Potential temperature
λ	Lyapunov exponent of the flow
λ_1, λ_2	Eigenvalues
ϕ	Parcel-pair orientation
χ	Local orientation of axis of nonrotation (i.e., orientation along which $\omega = 0$)
χ_c	Asymptotic contraction axis; also an axis of nonrotation
χ_d	Asymptotic dilatation axis; also an axis of nonrotation
ψ	Local orientation of the axes of dilatation (ψ_d) and contraction (ψ_c)
ψ_c	Local orientation of the axis of contraction (ψ_c)
ψ_d	Local orientation of the axis of dilatation (ψ_d)
ω	Rotation rate of separation vector
Ω_+	Maximum instantaneous counterclockwise rotation rate, $\omega _{\phi=\psi_d+\pi/4}$
Ω_-	Maximum instantaneous clockwise rotation rate, $\omega _{\phi=\psi_d-\pi/4}$
Ω^2	Product of Ω_+ and Ω_-
$ \nabla Q $	Horizontal gradient of Q

APPENDIX B

Derivation of the Instantaneous Local Lyapunov Exponent

The longer-term evolution of the flow field can be solved by taking the eigenvalues λ of (4). Written in matrix form, (4) becomes

$$\frac{d}{dt} \begin{pmatrix} \delta x \\ \delta y \end{pmatrix} = \begin{pmatrix} \frac{\partial u}{\partial x} & \frac{\partial u}{\partial y} \\ \frac{\partial v}{\partial x} & \frac{\partial v}{\partial y} \end{pmatrix} \begin{pmatrix} \delta x \\ \delta y \end{pmatrix}. \quad (\text{B1})$$

The eigenvalues are obtained by solving

$$\det \begin{vmatrix} \frac{\partial u}{\partial x} - \lambda & \frac{\partial u}{\partial y} \\ \frac{\partial v}{\partial x} & \frac{\partial v}{\partial y} - \lambda \end{vmatrix} = 0,$$

which provides the following quadratic equation in λ :

$$\lambda^2 - \lambda \left(\frac{\partial u}{\partial x} + \frac{\partial v}{\partial y} \right) + J(u, v) = 0, \quad (\text{B2})$$

where $J(u, v)$ is the Jacobian of the wind field:

$$J(u, v) = \det \begin{vmatrix} \frac{\partial u}{\partial x} & \frac{\partial u}{\partial y} \\ \frac{\partial v}{\partial x} & \frac{\partial v}{\partial y} \end{vmatrix} = \frac{\partial u}{\partial x} \frac{\partial v}{\partial y} - \frac{\partial u}{\partial y} \frac{\partial v}{\partial x}. \quad (\text{B3})$$

The Jacobian can be written in terms of the four basic kinematic quantities (i.e., D , ζ , E_{st} , and E_{sh}). In particular, simple relationships exist between their squares:

$$D^2 = \left(\frac{\partial u}{\partial x} \right)^2 + \left(\frac{\partial v}{\partial y} \right)^2 + 2 \frac{\partial u}{\partial x} \frac{\partial v}{\partial y},$$

$$\zeta^2 = \left(\frac{\partial u}{\partial y} \right)^2 + \left(\frac{\partial v}{\partial x} \right)^2 - 2 \frac{\partial u}{\partial y} \frac{\partial v}{\partial x},$$

$$E_{st}^2 = \left(\frac{\partial u}{\partial x} \right)^2 + \left(\frac{\partial v}{\partial y} \right)^2 - 2 \frac{\partial u}{\partial x} \frac{\partial v}{\partial y},$$

$$E_{sh}^2 = \left(\frac{\partial u}{\partial y} \right)^2 + \left(\frac{\partial v}{\partial x} \right)^2 + 2 \frac{\partial u}{\partial y} \frac{\partial v}{\partial x}.$$

Combining the first two relationships gives the intermediate expression

$$D^2 + \zeta^2 = E_{st}^2 + E_{sh}^2 + 4 \left(\frac{\partial u}{\partial x} \frac{\partial v}{\partial y} - \frac{\partial u}{\partial y} \frac{\partial v}{\partial x} \right), \quad (\text{B4})$$

or

$$D^2 + \zeta^2 - E^2 = 4J(u, v). \quad (\text{B5})$$

Consequently, (B2) becomes

$$\lambda^2 - D\lambda + \frac{D^2 + \zeta^2 - E^2}{4} = 0, \quad (\text{B6})$$

which, as a quadratic equation for λ , can be solved to give two solutions:

$$\lambda_1 = \frac{1}{2} [D + (E^2 - \zeta^2)^{1/2}], \quad (\text{B7a})$$

$$\lambda_2 = \frac{1}{2} [D - (E^2 - \zeta^2)^{1/2}]. \quad (\text{B7b})$$

Equation (B7a) is the same as (21a), and (B7b) is the same as the negative of (21b). This appendix demonstrates that the instantaneous local Lyapunov exponent is equivalent to the asymptotic dilatation rate \mathcal{D} or the negative of the asymptotic contraction rate \mathcal{C} .

REFERENCES

- Barnes, S. L., and B. R. Colman, 1993: Quasigeostrophic diagnosis of cyclogenesis associated with a cutoff extratropical cyclone—The Christmas 1987 storm. *Mon. Wea. Rev.*, **121**, 1613–1634.
- , and —, 1994: Diagnosing an operational numerical model using Q -vector and potential vorticity concepts. *Wea. Forecasting*, **9**, 85–102.
- Batchelor, G. K., 1952: The effect of homogeneous turbulence on material lines and surfaces. *Proc. Roy. Soc.*, **A213**, 349–366.
- Benzi, R., S. Patarnello, and P. Santangelo, 1988: Self-similar coherent structures in two-dimensional decaying turbulence. *J. Phys. A: Math. Gen.*, **21**, 1221–1237.
- Bergeron, T., 1928: Über die dreidimensional verknüpfende Wetteranalyse I. *Geophys. Publ.*, **5** (6), 1–111.
- Bishop, C. H., 1996: Domain-independent attribution. Part II: Its value in the verification of dynamical theories of frontal waves and frontogenesis. *J. Atmos. Sci.*, **53**, 253–262.
- Bjerknes, J., and H. Solberg, 1922: Life cycle of cyclones and the polar front theory of atmospheric circulation. *Geophys. Publ.*, **3** (1), 3–18.
- Browning, K. A., 1986: Conceptual models of precipitation systems. *Wea. Forecasting*, **1**, 23–41.
- , 1990: Organization of clouds and precipitation in extratropical cyclones. *Extratropical Cyclones: The Erik Palmén Memorial Volume*, C. W. Newton and E. O. Holopainen, Eds., Amer. Meteor. Soc., 129–153.
- Carlson, T. N., 1980: Airflow through midlatitude cyclones and the comma cloud pattern. *Mon. Wea. Rev.*, **108**, 1498–1509.
- Cohen, R. A., and C. W. Kreitzberg, 1997: Airstream boundaries in numerical weather simulations. *Mon. Wea. Rev.*, **125**, 168–183.
- Cunningham, P., and D. Keyser, 2000: Analytical and numerical modelling of jet streaks: Barotropic dynamics. *Quart. J. Roy. Meteor. Soc.*, **126**, 3187–3217.
- , and —, 2004: Dynamics of jet streaks in a stratified quasigeostrophic atmosphere: Steady-state representations. *Quart. J. Roy. Meteor. Soc.*, **130**, 1579–1609.
- Davies-Jones, R., 1985: Comments on “A kinematic analysis of frontogenesis associated with a nondivergent vortex.” *J. Atmos. Sci.*, **42**, 2073–2075.
- Doswell, C. A., III, 1984: A kinematic analysis of frontogenesis associated with a nondivergent vortex. *J. Atmos. Sci.*, **41**, 1242–1248.
- , 1985: Reply. *J. Atmos. Sci.*, **42**, 2076–2079.
- Fairlie, T. D., R. B. Pierce, J. A. Al-Saadi, W. L. Grose, J. M. Russell III, M. H. Proffitt, and C. R. Webster, 1999: The contribution of mixing in Lagrangian photochemical predictions of polar ozone loss over the Arctic in summer 1997. *J. Geophys. Res.*, **104**, 26 597–26 609.
- Hoskins, B. J., 1982: The mathematical theory of frontogenesis. *Annu. Rev. Fluid Mech.*, **14**, 131–151.
- , and N. V. West, 1979: Baroclinic waves and frontogenesis. Part II: Uniform potential vorticity jet flows—Cold and warm fronts. *J. Atmos. Sci.*, **36**, 1663–1680.
- , I. Draghici, and H. C. Davies, 1978: A new look at the ω -equation. *Quart. J. Roy. Meteor. Soc.*, **104**, 31–38.
- Keyser, D., 1999: On the representation and diagnosis of frontal circulations in two and three dimensions. *The Life Cycles of Extratropical Cyclones*, M. A. Shapiro and S. Grønås, Eds., Amer. Meteor. Soc., 239–264.
- , M. J. Reeder, and R. J. Reed, 1988: A generalization of

- Petterssen's frontogenesis function and its relation to the forcing of vertical motion. *Mon. Wea. Rev.*, **116**, 762–780.
- Kundu, P. K., 1990: *Fluid Mechanics*. Academic Press, 638 pp.
- MacVean, M. K., and J. D. Woods, 1980: Redistribution of scalars during upper ocean frontogenesis: A numerical model. *Quart. J. Roy. Meteor. Soc.*, **106**, 293–311.
- McWilliams, J. C., 1984: The emergence of isolated coherent vortices in turbulent flow. *J. Fluid Mech.*, **146**, 21–43.
- Miller, J. E., 1948: On the concept of frontogenesis. *J. Meteor.*, **5**, 169–171.
- Muller, B. M., and H. E. Fuelberg, 1990: A simulation and diagnostic study of water vapor image dry bands. *Mon. Wea. Rev.*, **118**, 705–722.
- Parker, D. J., 1999: Passage of a tracer through frontal zones: A model for the formation of forward-sloping cold fronts. *Quart. J. Roy. Meteor. Soc.*, **125**, 1785–1800.
- Petterssen, S., 1936: Contribution to the theory of frontogenesis. *Geophys. Publ.*, **11** (6), 1–27.
- , 1940: *Weather Analysis and Forecasting*. McGraw-Hill, 505 pp.
- , 1953: On the relation between vorticity, deformation and divergence and the configuration of the pressure field. *Tellus*, **5**, 231–237.
- , 1956: *Motion and Motion Systems*. Vol. 1, *Weather Analysis and Forecasting*. 2d ed. McGraw-Hill, 428 pp.
- Pierrehumbert, R. T., and H. Yang, 1993: Global chaotic mixing on isentropic surfaces. *J. Atmos. Sci.*, **50**, 2462–2480.
- Rotunno, R., W. C. Skamarock, and C. Snyder, 1994: An analysis of frontogenesis in numerical simulations of baroclinic waves. *J. Atmos. Sci.*, **51**, 3373–3398.
- Sanders, F., 1999: A proposed method of surface map analysis. *Mon. Wea. Rev.*, **127**, 945–955.
- Saucier, W. J., 1955: *Principles of Meteorological Analysis*. University of Chicago Press, 438 pp.
- Schubert, W. H., M. T. Montgomery, R. K. Taft, T. A. Guinn, S. R. Fulton, J. P. Kossin, and J. P. Edwards, 1999: Polygonal eyewalls, asymmetric eye contraction, and potential vorticity mixing in hurricanes. *J. Atmos. Sci.*, **56**, 1197–1223.
- Schultz, D. M., 2004: Cold fronts with and without prefrontal wind shifts in the central United States. *Mon. Wea. Rev.*, **132**, 2040–2053.
- , D. Keyser, and L. F. Bosart, 1998: The effect of large-scale flow on low-level frontal structure and evolution in midlatitude cyclones. *Mon. Wea. Rev.*, **126**, 1767–1791.
- Smith, R. K., W. Ulrich, and G. Dietachmayer, 1990: A numerical study of tropical cyclone motion using a barotropic model. I: The role of vortex asymmetries. *Quart. J. Roy. Meteor. Soc.*, **116**, 337–362.
- Vuorela, L. A., 1953: A synoptic study of deformation fields. *Tellus*, **5**, 413–419.
- Welander, P., 1955: Studies on the general development of motion in a two-dimensional, ideal fluid. *Tellus*, **7**, 141–156.
- Wernli, H., 1997: A Lagrangian-based analysis of extratropical cyclones. II: A detailed case-study. *Quart. J. Roy. Meteor. Soc.*, **123**, 1677–1706.
- , and H. C. Davies, 1997: A Lagrangian-based analysis of extratropical cyclones. I: The method and some applications. *Quart. J. Roy. Meteor. Soc.*, **123**, 467–489.
- Xu, Q., 1988: Baroclinic waves and frontogenesis with an embedded zone of small moist symmetric stability. *Quart. J. Roy. Meteor. Soc.*, **114**, 1221–1251.
- , 1990: Cold and warm frontal circulations in an idealized moist semigeostrophic baroclinic wave. *J. Atmos. Sci.*, **47**, 2337–2352.
- , 1992: A geostrophic pseudovorticity and geostrophic C-vector forcing—A new look at the Q vector in three dimensions. *J. Atmos. Sci.*, **49**, 981–990.
- Zeng, X., R. A. Pielke, and R. Eykholt, 1993: Chaos theory and its applications to the atmosphere. *Bull. Amer. Meteor. Soc.*, **74**, 631–644.